CHEMISTRY

Accelerating ion transport in polycrystalline conductors: On pores and grain boundaries

Erica Truong[1,2]†, Sawankumar V. Patel[1,2]†, Haoyu Liu[1], Yudan Chen[1,2], Valentina Lacivita[3], Chi Zhang[4], Ifeoluwa P. Oyekunle[1,2], Islamiyat Ojelade[1,2], Yongkang Jin[1,2], Brendon T. Jones[5], Lincoln J. Miara[3], Vinayak P. Dravid[4], Hanwei Gao[5], Ryounghee Kim[6], Yan Wang[3], Yan-Yan Hu[1,2]*

Polycrystalline ion conductors are widely used as solid electrolytes in energy storage technologies. However, they often exhibit poor ion transport across grain boundaries and pores. This work demonstrates that strategically tuning the mesoscale microstructures, including pore size, pore distribution, and chemical compositions of grain boundaries, can improve ion transport. Using $LiTa_2PO_8$ as a case study, we have shown that the combination of LiF as a sintering agent with Hf^{4+} implantation improves grain-grain contact, resulting in smaller, evenly distributed pores, reduced chemical contrast, and minimized nonconductive impurities. A suite of techniques has been used to decouple the effects of LiF and Hf^{4+}. Specifically, LiF modifies particle shape and breaks large pores into smaller ones, while Hf^{4+} addresses the chemical mismatches between grains and grain boundaries. Consequently, this approach achieves nearly two orders of magnitude improvement in ion conduction. Tuning mesoscale structures offers a cost-effective method for enhancing ion transport in polycrystalline systems and has notable implications for synthesizing high-performance ionic materials.

INTRODUCTION

Ion conduction in polycrystalline materials occurs in grains and across grain boundaries. Most polycrystalline ion conductors suffer from poor ion transport across grain boundaries. Elevated activation energy barriers across grain boundaries are the primary factor, leading to grain boundary conductivity one to three orders of magnitude lower than bulk conductivity (*1*, *2*). For example, $LiTa_2PO_8$, discovered by Kim *et al.* (*3*), shows an impressive room-temperature bulk ionic conductivity of 1.66 mS cm^{-1}, among the highest in the oxide class of solid electrolytes. However, this oxide material suffers from poor Li^+ transport across grain boundaries. As a result, the total ionic conductivity, 0.02 mS cm^{-1}, is two orders of magnitude lower than the bulk conductivity. Therefore, it is crucial to determine and modify the grain boundaries and other mesoscale microstructures to enhance the overall conductivity (*4*–*6*).

A crystallographic grain boundary is defined as a lattice defect because of a mismatch at the crystallite/grain interfaces, with the thickness ranging from 0.2 to 1 nm (*1*, *2*). Grain boundaries could be considered a lattice mismatch between two grains of the same phase or generated because of secondary phases. In both cases, the ion transport in the grain boundary regions is often severely hindered (*7*). One major factor attributed to poor grain boundary conduction is extended defects such as microcracks and porosity, which correlate with the ion conduction and overall performance in polycrystalline ion conductors (*8*). The most common relationship is that electrolytes of low porosity and high density exhibit improved ionic conductivity compared to electrolytes with high porosity and low density. Grain boundaries are believed to be the source of these defects because of their low fracture toughness compared to the bulk (*9*, *10*). Therefore, the inherent route to improve ion conduction of polycrystalline materials is to minimize extended defects, yet this entails high-temperature sintering and other more stringent syntheses at a high cost. In addition, extended defects in high-density materials are often generated during device operation.

Fortunately, ion transport in polycrystalline materials can be improved without eliminating extended defects. Polycrystalline materials are often influenced by collective or emergent behaviors, such as the interactions between grains and pores. This is well demonstrated in the work by Lin *et al.* (*8*), which shows that the absolute porosity or density of a material does not necessarily correlate with poor ion transport. Therefore, mesoscale structural features, such as the distribution and size of the pores and grain boundaries, can be tuned to facilitate ion transport. Furthermore, the composition at grain boundaries has been shown to play a notable role in ion transport. Xu *et al.*'s study (*4*) identified trace impurities at grain boundaries to be the likely major source of grain boundary charge. The aforementioned positive grain boundary core causes the depletion of lithium ions in adjacent space charge layers (*11*, *12*) and thus creates a gradient in the concentration profile of lithium ions across grain boundaries, leading to a reduced number of charge carriers at grain boundaries, which impedes ion transport (*13*). Therefore, harnessing the chemical tunability of grain boundaries presents another venue for enhancing ion transport in polycrystalline solid electrolytes.

To understand the impact of mesoscale structures on ion conduction, we varied the pore size, distribution, and grain boundary chemical compositions of $LiTa_2PO_8$ with Hf^{4+} doping combined with LiF-assisted sintering and examined its ion transport properties. Overall, with advanced characterizations of the structures and ion dynamics, we found that adding Hf^{4+} and LiF not only mitigates differences in chemical composition but also alters the pore size and distribution. As

[1]Department of Chemistry and Biochemistry, Florida State University, Tallahassee, FL, 32306, USA. [2]Center of Interdisciplinary Magnetic Resonance, National High Magnetic Field Laboratory, 1800 East Paul Dirac Drive, Tallahassee, FL 32310, USA. [3]Advanced Materials Lab, Samsung Advanced Institute of Technology-America, Samsung Semiconductor, Inc., Cambridge, MA 02138, USA. [4]Materials Science and Engineering, Northwestern University, Evanston, IL, 60208, USA. [5]Department of Physics, Florida State University, Tallahassee, FL, 32306, USA. [6]Battery Material Lab, Material Research Center, Samsung Advanced Institute of Technology (SAIT), Samsung Electronics Co., Ltd., 130 Samsung-ro, Yeongtong-gu, Suwon-si, Geyonggi-do 16678 Republic of Korea.
*Corresponding author. Email: yhu@fsu.edu
†These authors contributed equally to this work.

a result, we observed improved grain boundary ion transport and enhanced the overall ionic conductivity from 0.02 to 0.79 mS cm^{-1}. The insights gained from this work will provide guidance on leveraging mesoscale structures for enhanced material performance.

RESULTS

Structures via neutron diffraction and pair distribution function analysis

The structures and phase stability of $LiTa_2PO_8$, $Li_{1.05}Hf_{0.05}Ta_{1.95}PO_8$, and $Li_{1.05}Hf_{0.05}Ta_{1.95}PO_8$-0.15LiF were examined using high-resolution neutron and x-ray powder diffraction. Hereafter, the samples will be denoted as follows: $LiTa_2PO_8$ (LTPO), $LiTa_2PO_8$-0.15LiF (LTPO-LiF), $Li_{1.05}Hf_{0.05}Ta_{1.95}PO_8$ (LHTPO), and $Li_{1.05}Hf_{0.05}Ta_{1.95}PO_8$-0.15LiF (LHTPO-LiF). Figure 1A displays the crystal structure of the LHTPO. The framework consists of corner-shared polyhedra of TaO_6 and PO_4 located in fully occupied crystallographic sites. Tantalum (Ta) occupies three Wyckoff sites, i.e., 4a, 4e, and 8f, whereas phosphorus occupies 8f. Lithium ions partially occupy four interstitial sites (tables S1 to S3 and fig. S1A). Rietveld refinement of the diffraction data on LTPO (fig. S2), LHTPO (fig. S3), and LHTPO-LiF (Fig. 1, B to D) was implemented to determine the changes in unit cell parameters upon hafnium doping. All the peaks match the monoclinic space group *C*/2*c* (space group no. 15) with an R_{wp} of 4.513. Hf partially replaces Ta at the Wyckoff 4a sites. Note that F was not considered in the refinement because it was removed during the high-temperature treatment, confirmed with ^{19}F nuclear magnetic resonance (NMR) (fig. S4). Table 1 reports the changes in unit cell parameters and volume upon hafnium doping. An increase in lattice volume upon hafnium doping indicates the successful incorporation of hafnium in the structure. This is expected as Hf^{4+} exhibits a larger ionic radius than Ta^{5+} with a difference of ~0.1 Å.

The doping limit of Hf^{4+} in the $Li_{1+x}Hf_xTa_{2-x}PO_8$ structure was $x \sim 0.05$ (fig. S1B). Such a low doping limit is due to the formation of a competing NASICON (sodium superionic conductor) phase of $LiHf_2(PO_4)_3$ that is thermodynamically stable, which was also confirmed by ^{31}P NMR (fig. S5). Using the convex hull minimum energy reference, the thermodynamic energy impact of substituting Ta^{5+} with Hf^{4+} was evaluated with density functional theory (DFT)–calculated phase diagrams. The energy above the hull increases upon Hf^{4+} doping, as represented in Table 2. This illustrates that incorporating Hf^{4+} in the bulk structure of $LiTa_2PO_8$ is energetically unfavorable, which explains the poor doping limit.

The neutron pair distribution function (nPDF) $G(r)$ was obtained to determine the local structural changes induced by Hf^{4+} doping. Figure 2A represents the nPDF with the corresponding atom pairs determined from the refined structure using Bragg diffraction. The peak between 1.52 and 1.54 Å represents the P–O pair in the PO_4 tetrahedra, which exhibits no notable change other than a slight increase in the average P–O distance from 1.52 to 1.54 Å because of Hf^{4+} doping (fig. S6). The peak at around 1.95 Å corresponds to the Ta–O pair in the TaO_6 octahedra, whereas the shoulder peak around 2.05 Å corresponds to Hf–O in the HfO_6 octahedra. The ionic radius of hafnium in octahedral coordination is larger (0.71 Å) than that of tantalum (0.64 Å), resulting in longer Hf–O bonds. A reduction in the intensity of the Ta–O pair with an increase in the intensity of the Hf–O pair confirms the incorporation of hafnium in the structure (Fig. 2B). Another key observation from the nPDF is the negative intensity peak at ~2.3 Å from Li–O pairs (Fig. 2C). The peak intensity increases and smears out upon Hf^{4+} doping, signifying lithium disorder and delocalization. Similar changes in the Li^+-anion pair have been observed in Cl- and Br-rich argyrodites that correlate the lithium delocalization with fast Li^+-ion conduction (*14*). Figure 2D shows the real-space PDF refinement using the structural parameters

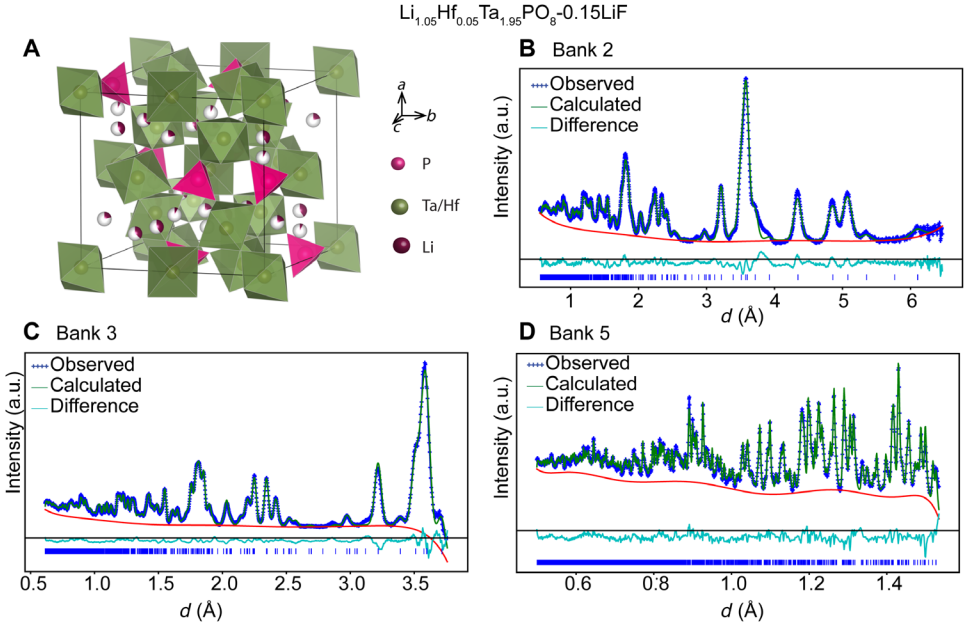

Fig. 1. Average structure of $Li_{1.05}Hf_{0.05}Ta_{1.95}PO_8$-0.15LiF, obtained from the Rietveld refinement of the neutron diffraction data. LiF is a sintering additive and leaves no trace in the structure. (**A**) Polyhedral connectivity of TaO_6 and PO_4 in the $LiTa_2PO_8$ framework. Rietveld refinement of the neutron diffraction pattern for $Li_{1.05}Hf_{0.05}Ta_{1.95}PO_8$-0.15LiF: (**B**) Bank 2, (**C**) Bank 3, and (**D**) Bank 5. a.u., arbitrary units.

Table 1. Unit cell parameters of $Li_{1+x}Hf_xTa_{2-x}PO_8$ compositions. Results were calculated from Rietveld refinement.

Sample	*a* (Å)	*b* (Å)	*C* (Å)	β (°)	vol (Å^3)
$LiTa_2PO_8$	9.7091	11.5339	10.7079	89.967	1199.105
$Li_{1.05}Hf_{0.05}Ta_{1.95}PO_8$	9.7131	11.5363	10.7089	89.920	1199.970
$Li_{1.05}Hf_{0.05}Ta_{1.95}PO_8$-0.15LiF	9.7171	11.5374	10.7101	89.954	1200.723

Table 2. Energy above hull (meV/atom) of the $Li_{1+x}Hf_xTa_{2-x}PO_8$ compositions. Results were calculated from a phase diagram analysis with experimentally reported phases in Materials Project.

$Li_{1+x}Hf_xTa_{2-x}PO_8$	Energy above hull (meV/atom)	Decomposition products
$x = 0$	16.4	Ta_2O_5, Li_3PO_4, $TaPO_5$
$x = 0.125$	19.8	Ta_2O_5, Li_3PO_4, $TaPO_5$, HfO_2
$x = 0.25$	24.5	Ta_2O_5, Li_3PO_4, $TaPO_5$, HfO_2
$x = 0.375$	29.4	Ta_2O_5, Li_3PO_4, $TaPO_5$, HfO_2

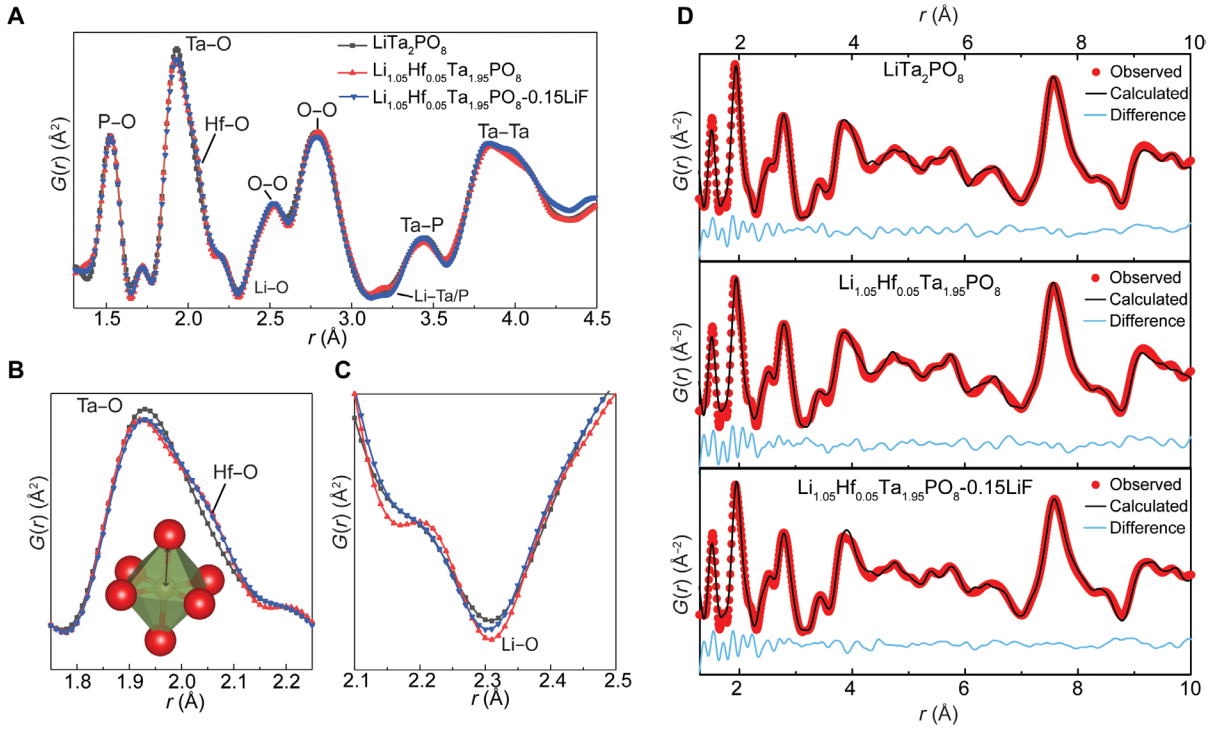

Fig. 2. Local structural analysis of $LiTa_2PO_8$, $Li_{1.05}Hf_{0.05}Ta_{1.95}PO_8$, and $Li_{1.05}Hf_{0.05}Ta_{1.95}PO_8$-0.15LiF. (**A**) nPDF of $LiTa_2PO_8$, $Li_{1.05}Hf_{0.05}Ta_{1.95}PO_8$, and $Li_{1.05}Hf_{0.05}Ta_{1.95}PO_8$-0.15LiF. (**B**) Local structural changes in the first near-neighbor coordination of Ta/Hf–O and (**C**) local structural changes in the first near-neighbor coordination of Li–O pairs. (**D**) PDF real space refinement from 1.3 to 10 Å using the monoclinic space group.

from Bragg refinement, and the results show that the local structure fits in the monoclinic space group.

Roles of LiF and Hf in modifying the mesoscale structures

Scanning electron microscopy (SEM) was used to examine the morphology of synthesized solid electrolytes. Figure 3 shows the SEM images of LTPO and LHTPO-LiF under both secondary electrons (SEs) and backscattered electrons (BSEs). SE images shown in Fig. 3 (A and B) provide topological information about the surface. The LTPO (Fig. 3A) has more voids than the LHTPO-LiF sample (Fig. 3B). The BSE yield depends on the composition of the sample and the crystal orientation. Therefore, grain boundaries that are not detectable in SE images can be observed in BSE images (fig. S7). Figure 3 (C and D) shows zoomed-in BSE images of pristine LTPO and

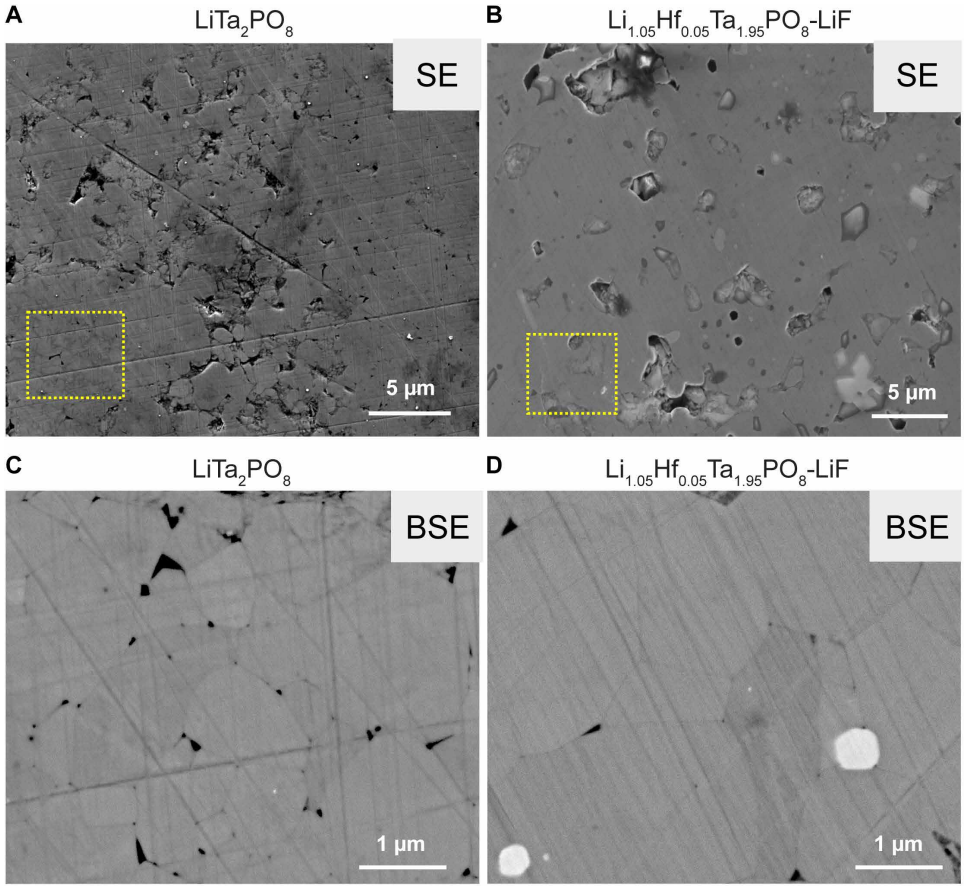

Fig. 3. SE and BSE SEM images of sintered $LiTa_2PO_8$ and $Li_{1.05}Hf_{0.05}Ta_{1.95}PO_8$-0.15LiF samples. SE images of (**A**) $LiTa_2PO_8$ and (**B**) $Li_{1.05}Hf_{0.05}Ta_{1.95}PO_8$-0.15LiF. Zoomed-in BSE images of the marked areas in (**C**) $LiTa_2PO_8$ and (**D**) $Li_{1.05}Hf_{0.05}Ta_{1.95}PO_8$-0.15LiF, revealing the grain boundaries. $Li_{1.05}Hf_{0.05}Ta_{1.95}PO_8$-0.15LiF exhibits fewer and less visible grain boundaries compared with $LiTa_2PO_8$.

LHTPO-LiF, respectively. The average grain size in pristine LTPO is smaller, ranging from 0.2 to 1.6 μm (Fig. 3C), compared to LHTPO-LiF (Fig. 3D), which ranges from 1 to 5 μm. A statistical analysis from multiple areas is provided in fig. S8. A larger grain size reduces the grain-to-grain contact area, minimizing the grain boundary per unit volume and apparent voids between grains. Moreover, a difference in the contrast between grain and grain boundaries is also observed. The grain boundaries are visible in the LTPO sample (Fig. 3C). In contrast, in LHTPO-LiF (Fig. 3D), the grain boundaries are not apparent from the seemingly smoother surface, which indicates a lesser deviation of the grain boundary composition from the grains. Therefore, adding Hf^{4+} and LiF plays a key role in modifying the chemical composition and morphology, specifically grain size and contact, of grain boundaries.

To further examine the role of Hf^{4+} and LiF in shaping the morphology of LHTPO particles, we compared SEM/energy-dispersive x-ray spectroscopy (EDS) maps of LTPO, LTPO-LiF, LHTPO, and LHTPO-LiF (fig. S9). From the SEM images, the presence of voids is apparent for LTPO, LTPO-LiF, and LHTPO, while LHTPO-LiF shows fewer large voids with smooth cross sections. This observation exemplifies the importance of both Hf^{4+} and LiF for minimizing large voids and grain boundary formation. Comparing LTPO and LTPO-LiF, the number of large voids decreased with the addition of LiF (fig. S9, A and B). LiF, with a low melting point, aids in particle compaction and reduces large pores (*15*). Any residual LiF is removed via sublimation during the final sintering step at ~1050°C (fig. S4) (*16*). The corresponding EDS images for LTPO-LiF reveal that the remaining small pores shown in the SEM image are occupied by the Li_3PO_4 and $LiPO_3$ impurity phases (fig. S9B).

The role of Hf^{4+} is twofold: minimizing pore size and promoting large grain formation. These two effects are likely correlated because Figure 3 (C and D) unveils that pores form at grain boundaries, especially at trijunctions. Fewer grain boundaries will yield fewer pores of large size. From the LHTPO SEM/EDS images (fig. S9c), the morphology and composition are more uniform than those of LTPO and LTPO-LiF. However, many small pockets are still visible in LHTPO, of which the Ta concentration is relatively lower than Hf and P. These pockets are most likely filled with $LiHf_2(PO_4)_3$ and Hf-doped $LiTa_2PO_8$, supported by the Hf^{4+} distribution mainly around the grain boundaries and in the pores (fig. S10). Using the benefits of Hf^{4+} and LiF, the number of large defects and aggregated impurities in the LTPO system becomes nearly negligible (fig. S9D). In summary, with the addition of LiF, the grain-to-grain contact can be improved. Still, adding Hf^{4+} is necessary to further lessen grain boundary composition deviation from grains and minimize low-conductive phosphates.

This leads to an intriguing question: Do LiF and Hf^{4+} improve the pellet density of LTPO? From density measurements (Table 3),

Table 3. Pellet densities of $Li_{1+x}Hf_xTa_{2-x}PO_8$. Densities were calculated with respect to the theoretical density of $LiTa_2PO_8$ (5.85 g cm^{-3}).

Sample	Density (%)
$LiTa_2PO_8$	97.0
$LiTa_2PO_8$-0.15LiF	86.0
$Li_{1.05}Hf_{0.05}Ta_{1.95}PO_8$	91.7
$Li_{1.05}Hf_{0.05}Ta_{1.95}PO_8$-0.15LiF	85.5

LTPO exhibits the highest density, ~97% of the theoretical value, but the lowest ionic conductivity. LHTPO-LiF has the lowest density of ~85% but the highest ionic conductivity. Thus, ion transport is more influenced by the size and arrangement of the extended defects than by pellet density. As demonstrated, LiF and Hf^{4+} substantially modify the size and distribution of the pores and grain boundaries. The morphology of LTPO and LTPO-LiF is inconsistent and rough (fig. S9). However, with the incorporation of Hf^{4+}, the pellet surface is relatively uniform, and the impurities and voids are more evenly distributed compared to LTPO and LTPO-LiF. This was shown to be beneficial as the activation energy for ion transport at grain boundaries decreased from 0.46 to 0.35 eV for LTPO and LHTPO, respectively (table S4). The low contrast in chemical composition and microstructures was shown to be more beneficial for grain boundary conduction than bulk. Therefore, Hf^{4+} influences the arrangement of defects and chemical composition of the grain boundaries, making it favorable for ion conduction.

Tracing Hf to the grain boundaries: High-resolution NMR

High-resolution ^{31}P NMR was acquired to probe local changes in the phosphorus local environment (*17*–*19*). Figure 4A shows the ^{31}P NMR of LTPO, LTPO-LiF, LHTPO, and LHTPO-LiF. On the basis of the crystal structure refinement, PO_4^{3-} of $LiTa_2PO_8$ occupies one crystallographic site, Wyckoff 8f. This is evident from the one ^{31}P resonance at ~−10 parts per million (ppm) in the LTPO. The minor peak observed at 9.95 ppm is attributed to the Li_3PO_4 impurity phase (*20*, *21*). With the addition of LiF, additional impurity phases are observed with ^{31}P NMR resonances between −24 and −21 ppm, which are assigned to a mixture of crystalline and glassy $LiPO_3$ phases (*22*, *23*). Hafnium doping results in two additional peaks at −19 and −17 ppm, corresponding to the Hf-doped $LiTa_2PO_8$ and impurity phase $LiHf_2(PO_4)_3$, respectively (Fig. 4B). The assignment of the −17-ppm resonance was confirmed by the ^{31}P NMR of the synthesized pure NASICON phase $LiHf_2(PO_4)_3$ (fig. S5). The ^{31}P

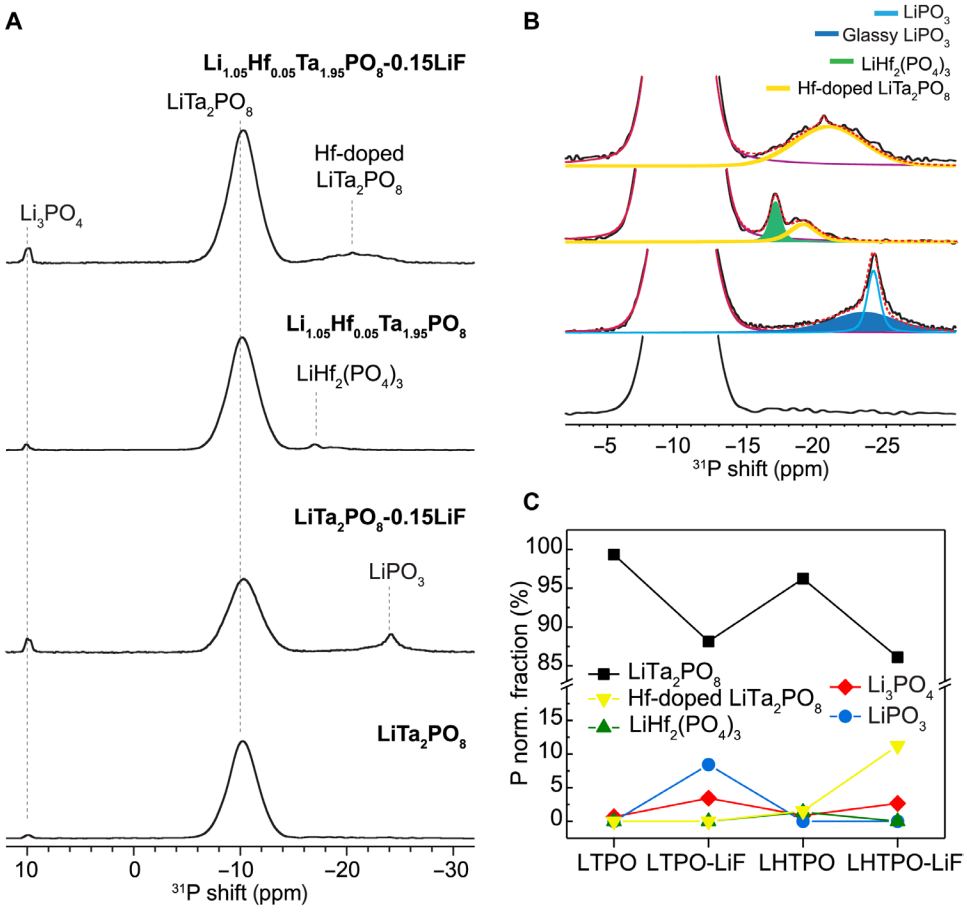

Fig. 4. PO_4^{3-} local structural environments in $LiTa_2PO_8$, $LiTa_2PO_8$-0.15LiF, $Li_{1.05}Hf_{0.05}Ta_{1.95}PO_8$, and $Li_{1.05}Hf_{0.05}Ta_{1.95}PO_8$-0.15LiF probed by ^{31}P NMR. (**A**) ^{31}P NMR spectra. (**B**) Zoomed-in ^{31}P NMR spectra to show the Hf-doped $LiTa_2PO_8$ peak. (**C**) Quantification of $LiTa_2PO_8$, Hf-doped $LiTa_2PO_8$, and impurity phases including Li_3PO_4 and $LiPO_3$.

NMR shifts of $LiTa_2PO_8$ and Hf-containing phases were validated with DFT NMR calculations (table S5). Quantification of the phases observed from ^{31}P NMR is shown in Fig. 4C. LiF, as a sintering aid, increases the incorporation of Hf^{4+} in the structure from ~3 to 11% and limits the formation of $LiHf_2(PO_4)_3$ and $LiPO_3$ (*23*). Results from solid-state NMR, nPDF, and EDS mapping all support the incorporation of Hf^{4+} in the structure. In addition, SEM/EDS of LHTPO shows that Hf^{4+} is distributed differently from Ta (fig. S10), showing clusters of Hf-concentrated areas, likely $LiHf_2(PO_4)_3$ impurity phases. In addition, the remaining Hf^{4+} seems to distribute evenly around the grain boundaries in both LHTPO and LHTPO-LiF (fig. S10). Using ^{31}P NMR T_1 relaxation experiments, the location of Hf^{4+} was also indirectly probed. The results are shown in Table 4. The T_1 value of $LiTa_2PO_8$ (−10 ppm) is three times larger than that of the Hf-doped $LiTa_2PO_8$ (−19 ppm). Such a difference in T_1 signifies that Hf^{4+} is incorporated into a distinct spatial location other than $LiTa_2PO_8$ grains. Combined with the results from SEM and EDS, Hf-doped $LiTa_2PO_8$ is most probably located at the grain boundaries.

High-resolution ^6Li NMR was acquired to investigate the effects of Hf^{4+} doping on the lithium structural environments. The crystal structure contains four crystallographic Wyckoff sites of the Li^+-ion that are partially occupied (table S1). However, because of the fast exchange of Li^+, the peaks coalesce into one. The ^6Li NMR of LTPO reveals a symmetric line shape that resonates at ~0.48 ppm (fig. S11). With the addition of LiF, a shoulder is observed at −0.31 ppm, which corresponds to Li_3PO_4 impurities. The resonance of the other impurity, $LiPO_3$, overlaps with the major resonance of LTPO (*24*, *25*). The line broadening decreases with addition of LiF and Hf^{4+} from 57 Hz for LTPO to 34 Hz for LHTPO and 25 Hz for LHTPO-LiF. ^6Li NMR suggests that <2% Hf doping substantially modifies the Li^+ local environments. The resonances of Hf-doped $LiTa_2PO_8$ and $LiTa_2PO_8$ are not resolved; this may be due to Li^+ exchange between these two phases, which requires close spatial proximity between $LiTa_2PO_8$ and Hf-doped $LiTa_2PO_8$ phases. Therefore, the small amount of Hf-doped $LiTa_2PO_8$ is likely located at the surfaces of $LiTa_2PO_8$ grains, i.e., grain boundaries. This position facilitates effective Li^+ exchange between these phases and stabilizes the metastable Hf^{4+} doping within $LiTa_2PO_8$ through disordered grain boundary structures in the LHTPO-LiF sample.

Table 4. ^{31}P NMR T_1 relaxation times of $Li_{1+x}Hf_xTa_{2-x}PO_8$.

Sample	$LiTa_2PO_8$ (s)	Hf-doped $LiTa_2PO_8$ (s)
$LiTa_2PO_8$	6.0	–
$LiTa_2PO_8$-0.15LiF	6.5	–
$Li_{1.05}Hf_{0.05}Ta_{1.95}PO_8$	6.1	2.6
$Li_{1.05}Hf_{0.05}Ta_{1.95}PO_8$-0.15LiF	5.4	2.0

Ion transport and dynamics

To understand the effects of hafnium incorporation on Li^+-ion transport, we conducted electrochemical impedance spectroscopy (EIS) measurements. Separating the contributions of bulk, grain boundary, and electrode to the total conductivity is complex and has been extensively studied, especially for oxide electrolytes (*26*–*29*). To clearly elucidate all the polarization contributions in solid electrolytes, a broad frequency range, 1×10^9 to $\sim 2 \times 10^9$ Hz, or performing temperature-dependent EIS measurements is necessary (*26*, *27*). We chose to do the latter. Figure 5A shows the room-temperature Nyquist plots of LTPO, LTPO-LiF, LHTPO, and LHTPO-LiF, with the temperature-dependent EIS measurements displayed in fig. S12. A zoomed-in figure of the Nyquist plot measured at −40°C for LTPO shows the two semicircles (fig. S13), corresponding to ion transport in the grain and across grain boundaries, respectively. Conductivities were determined from the Nyquist plots using the equivalent circuit models described in the Supplementary Materials (fig. S14) (*26*, *30*).

LTPO exhibits a high bulk conductivity of ~1.99 mS cm^{-1} and a total conductivity of 0.013 mS cm^{-1}. Bulk transport occurs at ~3 MHz, whereas grain boundary transport is detected at ~121 Hz. With the addition of LiF, the grain boundary transport of LTPO-LiF is detected at ~25 kHz and exhibits an improved conductivity of 0.073 mS cm^{-1}. On the other hand, LHTPO showed the timescale of grain boundary

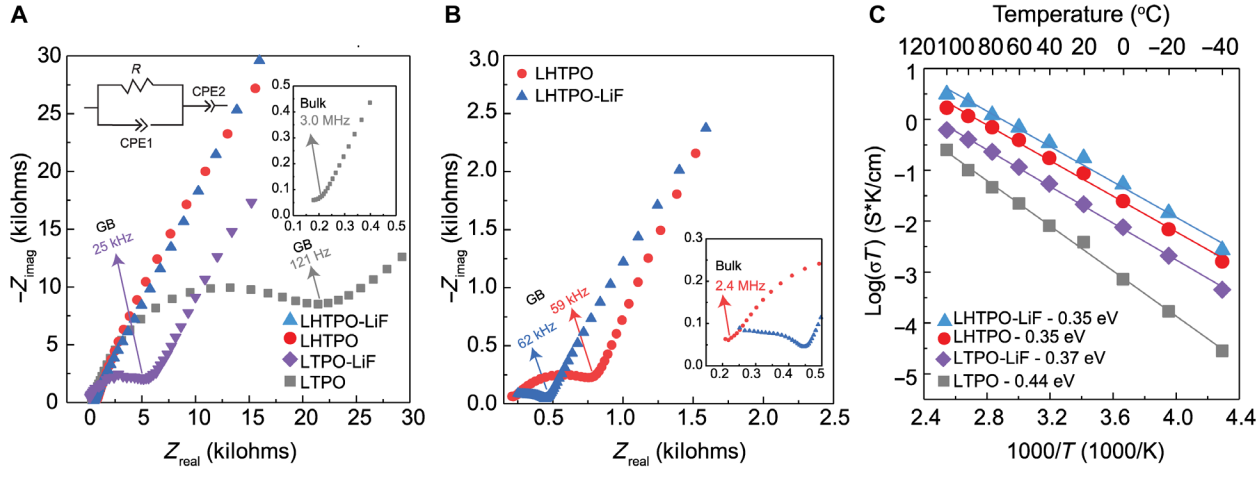

Fig. 5. Lithium-ion transport properties are determined via AC electrochemical impedance spectroscopy. (**A**) Room-temperature Nyquist plots of $LiTa_2PO_8$, $LiTa_2PO_8$-0.15LiF, $Li_{1.05}Hf_{0.05}Ta_{1.95}PO_8$, and $Li_{1.05}Hf_{0.05}Ta_{1.95}PO_8$-0.15LiF. The inset displays the part of the Nyquist plot related to the bulk ionic conductivity of $LiTa_2PO_8$. (**B**) Zoomed-in Nyquist plots of $Li_{1.05}Hf_{0.05}Ta_{1.95}PO_8$ and $Li_{1.05}Hf_{0.05}Ta_{1.95}PO_8$-0.15LiF. The extracted bulk and total ionic conductivities are listed in Table 5. (**C**) Arrhenius plots of total ionic conductivity.

Table 5. Room-temperature bulk and total ionic conductivities of $Li_{1+x}Hf_xTa_{2-x}PO_8$. Conductivities were determined using ac electrochemical impedance spectroscopy (Fig. 5).

Sample	σ_{Bulk} (mS cm^{-1})	σ_{Total} (mS cm^{-1})
$LiTa_2PO_8$	1.99	0.013
$LiTa_2PO_8$-0.15LiF	–	0.073
$Li_{1.05}Hf_{0.05}Ta_{1.95}PO_8$	1.72	0.43
$Li_{1.05}Hf_{0.05}Ta_{1.95}PO_8$-0.15LiF	–	0.79

transport occurring at ~60 kHz, signifying improved grain boundary conductivity (Fig. 5B). The overall ionic conductivity for LHTPO is 0.43 mS cm^{-1}, a 30-fold enhancement compared with that for LTPO. With Hf^{4+} doping and LiF-assisted sintering, total ion transport at grain boundaries is further enhanced and becomes indistinguishable from ion transport in bulk. As a result, the total ionic conductivity of LHTPO-LiF is further improved to 0.79 mS cm^{-1}. The room-temperature bulk and total conductivity values are presented in Table 5. The activation energies are calculated on the basis of the variable-temperature EIS measurements (fig. S12). Figure 5C shows that LHTPO-LiF has a lower activation energy (0.35 eV) than pristine LTPO (0.44 eV), thereby implying that not only does Hf^{4+} doping increase the overall ionic conductivity, but it also lowers the activation energy.

^{7}Li NMR T_1 relaxation times were measured to probe Li^+ dynamics (table S6). Since only one ^{7}Li resonance is resolved, the T_1 values reveal the average Li^+ dynamics. According to the Bloembergen, Purcell, and Pound model, the T_1 relaxation time is a function of motional rate ($\mathbf{1/\tau_c}$), as shown in Eq. 1 (*31*, *32*)

$$\left(\frac{1}{T_1}\right) = \frac{3\mu_o^2\gamma^4\hbar^2}{10r_0^6}\left[\frac{\tau_c}{1+\left(\omega_0\tau_c\right)^2}+\frac{4\tau_c}{1+4\left(\omega_o\tau_c\right)^2}\right] \quad (1)$$

where μ_o is the vacuum permeability, γ is the gyromagnetic ratio, $\hbar$ is the reduced Planck constant, r_o is the interatomic distance, and ω_o is the Larmor frequency. In the slow-motion regime ($\omega_o\tau_c >> 1$; ω_o = 116.64 MHz), T_1 decreases with increasing motional rate. In other words, faster ion motion is correlated with shorter T_1 relaxation times. To determine whether the T_1 values lie in this regime, we measured variable-temperature ^{7}Li NMR T_1 relaxation times for LHTPO-LiF (fig. S15). In fig. S15, the T_1 values decrease with increasing temperature, indicating that Li^+-ion motion in this material lies in the slow-motion regime of the Bloembergen, Purcell, and Pound model. LHTPO and LTPO-LiF exhibit larger T_1 values, signifying a relatively slower average Li^+ dynamics, possibly due to a notable amount of the low-conducting $LiHf_2(PO_4)_3$ and $LiPO_3$ impurity phases in LHTPO and LTPO-LiF, respectively. This aligns well with EIS measurements, in which the LHTPO-LiF shows the shortest T_1, indicating the fastest Li^+ dynamics among the four samples. This acceleration may be attributed to the enhanced Li^+ dynamics in the Hf-doped LTPO phase, where its participation in the global ion transport and exchange with Li^+ in LTPO elevates the overall Li^+-ion mobility.

DISCUSSION

The characteristics and distribution of pores and grain boundaries affect ion conduction in polycrystalline solid electrolytes. In this study, we leverage two strategies to alter the pore size, distribution, and chemical composition of grain boundaries to accelerate ion transport in the representative $LiTa_2PO_8$. Pure $LiTa_2PO_8$ exhibits large pores and Li_3PO_4 impurities, thereby leading to poor ion conduction. We first break down the large pores into small ones and redistribute them by using a sintering agent, LiF; this speeds up ion transport with a lowered activation energy. The grain boundaries are then further "glued" together by Hf^{4+} incorporation, which mitigates the chemical difference between grain and grain boundaries and further elevates grain boundary ion transport. High-resolution SEM reveals larger grains with less visible grain boundaries in $Li_{1.05}Hf_{0.05}Ta_{1.95}PO_8$-0.15LiF compared with $LiTa_2PO_8$. High-resolution ^{31}P NMR, relaxometry measurements, and EDS mapping elucidate that Hf resides in the grain boundary regions. ^{7}Li NMR relaxometry measurements reveal enhanced average Li^+ - ion mobility in $Li_{1.05}Hf_{0.05}Ta_{1.95}PO_8$-0.15LiF, consistent with the EIS observation of the enhanced overall ionic conductivity. This work provides a practical and effective strategy to enhance ion conduction in polycrystalline solid electrolytes.

MATERIALS AND METHODS

Synthesis of $Li_{1+x}Hf_xTa_{2-x}PO_8$

Pristine and Hf-doped $LiTa_2PO_8$ were synthesized via the high-temperature solid-state method. Stoichiometric amounts of LiOH (Alfa Aesar, ≥99%), TaO_5 (Alfa Aesar, ≥99.85%), $(NH_4)_2HPO_4$ (Alfa Aesar, ≥98%), HfO_2 (Sigma-Aldrich, ≥99%), and LiF (Alfa Aesar, ≥99%) were stoichiometrically weighed in a 30-ml zirconia jar. Then, 10 mol % of excess LiOH was added to compensate for lithium loss at high temperatures. Mechanochemical wet milling was used to uniformly mix the powders in 2.5 ml of acetone using the SPEX 8000M miller. The wet powder was dried at 60°C to remove acetone and then sintered at 600°C for 8 hours. The sintered powder was milled again for 1 hour and then sintered at 1000°C for 8 hours. The sintered powder was finely ground and pressed uniaxially into 6-mm pellets for a final sintering step at 1050°C for 12 hours. All sintering steps were conducted under ambient air.

Solid-state NMR

All NMR experiments were performed using the Bruker Avance-III 500-MHz 89-mm-bore spectrometer at the National High Magnetic Field Laboratory. ^{6}Li, ^{7}Li, and ^{31}P magic angle spinning (MAS) NMR experiments were performed at Larmor frequencies of 73.6, 194.4, and 202.5 MHz, respectively. A single-pulse experiment was carried out to collect ^{6}Li and ^{7}Li NMR with π/2 pulse lengths of 4.75 and 3.35 μs, respectively. For ^{31}P NMR, a spin-echo pulse sequence was used with a π/2 pulse length of 4.2 μs. The ^{7}Li and ^{31}P T_1 relaxation times were determined using inversion recovery pulse sequence experiments. Samples were packed under air into 2.5-mm zirconia rotors and spun at a MAS speed of 25 kHz.

Variable-temperature ^{7}Li T_1 relaxation experiments were performed using the Bruker Avance-I 300-MHz 89-mm-bore spectrometer at a Larmor frequency of 116.64 MHz. The inversion recovery pulse sequence was used to determine the T_1 relaxation times with a π/2 pulse length of 2.62 μs. Experiments were collected at temperatures from 25° to 95°C at an interval of 10°C. Samples were packed under air into 4-mm zirconia rotors and spun at a MAS speed of 9 kHz. ^{6,7}Li NMR was calibrated using $LiCl_{(s)}$ at −1.1 ppm. ^{31}P NMR was calibrated using 85 wt % $H_3PO_{4(l)}$ at 0 ppm.

Scanning electron microscopy/energy-dispersive x-ray spectroscopy

Electron microscopy studies were carried out using a JEOL JSM-7900FLV scanning electron microscope with an accelerating voltage of 5 kV and a probe current of 80 mA. EDS studies were carried out using a JEOL JSM-IT800 SEM/EDX system with an accelerating voltage of 15.0 kV with a dwell time of 5 μs. The sintered pellets were polished and mounted with carbon tape on an aluminum stub.

Neutron scattering

Neutron scattering experiments were performed at the NOMAD beamline (BL-1B) at the Spallation Neutron Source at Oak Ridge National Laboratory. The pellets of ~0.6 g each were ground into a fine powder and packed into 3-mm capillary tubes. The experiments were conducted at room temperature with a 1-hour acquisition for each sample. The total scattering structure factor $S(Q)$ was obtained after the background subtraction and normalization of the data. Last, the $S(Q)$ was Fourier transformed to obtain the PDF $G(r)$, which was analyzed using PDFgui software.

Rietveld analysis

Average structure analysis on the Bragg data was performed using GSAS II software. The data from each detector bank (31.0°, 65.0°, 120.4°, and 150.1°) were refined simultaneously using the monoclinic space group. The Chebyshev background function and pseudo-Voigt peak profile using the Si standard were used to generate instrumental parameters.

Electrochemical measurements

The ionic conductivities were determined on the basis of ac impedance spectroscopy using the Gamry Analyzer Reference 600+ with a frequency range of 1 Hz to 5 MHz. Samples were pelletized using a 6-mm die mold set and pressed at 4.14 MPa using a hydraulic press. Gold was sputtered on both sides of the pellets as blocking electrodes. Variable-temperature impedance measurements were conducted using the CSZ Microclimate chamber within a temperature range of −40° to 120°C at 20°C intervals with an applied voltage of 10 mV.

DFT calculations

All DFT energy calculations and ab initio molecular dynamics simulations were performed in the Vienna Ab initio Simulation Package (VASP). Projector augmented wave potentials with a kinetic energy cutoff of 520 eV were used in all structural optimizations and total energy calculations, and the exchange and correlation functionals were described within Perdew-Burke-Ernzerhof generalized gradient approximation. An electrostatic energy criterion was applied to prescreen 10 lowest-energy structures with different Li^+/vacancy and Ta^{5+}/Hf^{4+} orderings based on the experimentally identified crystal structure of $LiTa_2PO_8$, which include partially occupied Li sites. The lowest-energy structure for each composition was obtained from DFT structure optimization for the 10 prescreen structures. The phase stability of each composition was evaluated by generating the convex hull formed by the ground-state phases in the chemical spaces defined by all of the elements in the material, including the dopant species. All of the experimentally identified crystalline phases in the specific chemical space were included and processed using the Pymatgen software package interfaced with the Materials Project database (*33*–*35*). Materials above the convex hull are expected to decompose into their nearest phase on the facet of the convex hull.

The supercells of Hf-doped $LiTa_2PO_8$ were built on the basis of the unit cell of $LiTa_2PO_8$ with eight times formula units. The compositions of the supercell models are $Li_9Hf_1Ta_{15}P_8O_{64}$, $Li_{10}Hf_2Ta_{14}P_8O_{64}$, $Li_{11}Hf_3Ta_{13}P_8O_{64}$, and $Li_{12}Hf_4Ta_{12}P_8O_{64}$. The DFT optimization structures are included in the Supplementary Materials (VASP xml files).

Supercells for $LiTa_2PO_8$ (2 by 1 by 1), $Li_{1.05}Hf_{0.05}Ta_{1.95}PO_8$ (2 by 1 by 1), and $LiHf_2(PO_4)_3$ (2 by 2 by 1) were constructed on the basis of their unit cell parameters using Pymatgen. The isotropic chemical shifts of the relaxed structures were then calculated using perturbation theory (*36*, *37*).

Supplementary Materials

The PDF file includes:

Tables S1 to S6
Figs. S1 to S15
Legend for data S1
References

Other Supplementary Material for this manuscript includes the following:

Data S1

REFERENCES AND NOTES

1. S. Yu, D. J. Siegel, Grain boundary contributions to Li-Ion transport in the solid electrolyte $Li_7La_3Zr_2O_{12}$ (LLZO). *Chem. Mater.* **29**, 9639–9647 (2017).
2. J. A. Dawson, P. Canepa, M. J. Clarke, T. Famprikis, D. Ghosh, M. S. Islam, Toward understanding the different influences of grain boundaries on ion transport in sulfide and oxide solid electrolytes. *Chem. Mater.* **31**, 5296–5304 (2019).
3. J. Kim, J. Kim, M. Avdeev, H. Yun, S.-J. Kim, $LiTa_2PO_8$: A fast lithium-ion conductor with new framework structure. *J. Mater. Chem. A* **6**, 22478–22482 (2018).
4. X. Xu, Y. Liu, J. Wang, D. Isheim, V. P. Dravid, C. Phatak, S. M. Haile, Variability and origins of grain boundary electric potential detected by electron holography and atom-probe tomography. *Nat. Mater.* **19**, 887–893 (2020).
5. F. Zhu, M. S. Islam, L. Zhou, Z. Gu, T. Liu, X. Wang, J. Luo, C.-W. Nan, Y. Mo, C. Ma, Single-atom-layer traps in a solid electrolyte for lithium batteries. *Nat. Commun.* **11**, 1828 (2020).
6. C. Wang, Z. Sun, Y. Zhao, B. Wang, C. Shao, C. Sun, Y. Zhao, J. Li, H. Jin, L. Qu, Grain boundary design of solid electrolyte actualizing stable all-solid-state sodium batteries. *Small* **17**, e2103819 (2021).
7. A. R. Symington, M. Molinari, J. A. Dawson, J. M. Statham, J. Purton, P. Canepa, S. C. Parker, Elucidating the nature of grain boundary resistance in lithium lanthanum titanate. *J. Mater. Chem. A* **9**, 6487–6498 (2021).
8. L. Lin, A. Ayyaswamy, Y. Zheng, A. Fan, B. S. Vishnugopi, P. P. Mukherjee, K. B. Hatzell, Nonintuitive role of solid electrolyte porosity on failure. *ACS Energy Lett.* **9**, 2387–2393 (2024).
9. W. Xie, Z. Deng, Z. Liu, T. Famprikis, K. T. Butler, P. Canepa, Effects of grain boundaries and surfaces on electronic and mechanical properties of solid electrolytes. *Adv. Energy Mater.* **14**, 2304230 (2024).
10. Z. Ning, D. S. Jolly, G. Li, R. D. Meyere, S. D. Pu, Y. Chen, J. Kasemchainan, J. Ihli, C. Gong, B. Liu, D. L. R. Melvin, A. Bonnin, O. Magdysyuk, P. Adamson, G. O. Hartley, C. W. Monroe, T. J. Marrow, P. G. Bruce, Visualizing plating-induced cracking in lithium-anode solid-electrolyte cells. *Nat. Mater.* **20**, 1121–1129 (2021).
11. R. Usiskin, J. Maier, Interfacial effects in lithium and sodium batteries. *Adv. Energy Mater.* **11**, 2001455 (2021).
12. J. Luo, Interfacial engineering of solid electrolytes. *J. Materiomics* **1**, 22–32 (2015).
13. Z. Ding, J. Li, J. Li, C. An, Review—Interfaces: Key issue to be solved for all solid-state lithium battery technologies. *J. Electrochem. Soc.* **167**, 070541 (2020).
14. S. V. Patel, S. Banerjee, H. Liu, P. Wang, P.-H. Chien, X. Feng, J. Liu, S. P. Ong, Y.-Y. Hu, Tunable lithium-ion transport in mixed-halide argyrodites $Li_{6-x}PS_{5-x}ClBr_x$: An unusual compositional space. *Chem. Mater.* **33**, 1435–1443 (2021).
15. Y. Liu, Q. Sun, D. Wang, K. Adair, J. Liang, X. Sun, Development of the cold sintering process and its application in solid-state lithium batteries. *J. Power Sources* **393**, 193–203 (2018).
16. R. S. Scheffee, J. L. Margrave, Vapor pressure equations for species over solid and liquid LiF. *J. Chem. Phys.* **31**, 1682–1683 (1959).
17. X. Feng, P.-H. Chien, S. Patel, Y. Wang, Y.-Y. Hu, Enhanced ion conduction in $Li_{2.5}Zn_{0.25}PS_4$ via anion doping. *Chem. Mater.* **32**, 3036–3042 (2020).
18. X. Feng, P.-H. Chien, Y. Wang, S. Patel, P. Wang, H. Liu, M. Immediato-Scuotto, Y.-Y. Hu, Enhanced ion conduction by enforcing structural disorder in Li-deficient argyrodites $Li_{6-x}PS_{5-x}Cl_{1+x}$. *Energy Storage Mater.* **30**, 67–73 (2020).

19. P. Wang, H. Liu, S. Patel, X. Feng, P.-H. Chien, Y. Wang, Y.-Y. Hu, Fast ion conduction and its origin in $Li_{6-x}PS_{5-x}Br_{1+x}$. *Chem. Mater.* **32**, 3833–3840 (2020).
20. Y. Deng, C. Eames, J.-N. Chotard, F. Lalere, V. Seznec, S. Emge, O. Pecher, C. P. Grey, C. Masquelier, M. S. Islam, Structural and mechanistic insights into fast lithium-ion conduction in Li_4SiO_4–Li_3PO_4 solid electrolytes. *J. Am. Chem. Soc.* **137**, 9136–9145 (2015).
21. T. Asai, S. Kawai, NMR study of Li^+-ion diffusion in the solid solution $Li_{3+x}(P_{1-x}, Si_x)O_4$> with the γII-$Li_3PO_4$ structure. *Solid State Ion.* **7**, 43–47 (1982).
22. S. V. Dvinskikh, I. V. Murin, A. F. Privalov, A. A. Pronkin, E. Rossler, H.-M. Vieth, Microscopic structure of the glassy ionic conductor $x \cdot LiF + (1 - x) \cdot LiPO_3$ from NMR data. *J. Non Cryst. Solids* **240**, 79–90 (1998).
23. M. A. T. Marple, T. A. Wynn, D. Cheng, R. Shimizu, H. E. Mason, Y. S. Meng, Local structure of glassy lithium phosphorus oxynitride thin films: A combined experimental and ab initio approach. *Angew. Chem. Int. Ed.* **59**, 22185–22193 (2020).
24. T. M. Alam, T. J. Boyle, R. K. Brow, S. Conzone, ^6Li, ^7Li nuclear magnetic resonance investigation of lithium coordination in binary phosphate glasses. *J. Non Cryst. Solids* **258**, 140–154 (1999).
25. G. Zhong, J. Bai, P. N. Duchesne, M. J. McDonald, Q. Li, X. Hou, J. A. Tang, Y. Wang, W. Zhao, Z. Gong, P. Zhang, R. Fu, Y. Yang, Copper phosphate as a cathode material for rechargeable Li batteries and its electrochemical reaction mechanism. *Chem. Mater.* **27**, 150724095450003 (2015).
26. P. Braun, C. Uhlmann, A. Weber, H. Stormer, D. Gerthsen, E. Ivers-Tiffee, Separation of the bulk and grain boundary contributions to the total conductivity of solid lithium-ion conducting electrolytes. *J. Electroceramics* **38**, 157–167 (2017).
27. W. E. Tenhaeff, E. Rangasamy, Y. Wang, A. P. Sokolov, J. Wolfenstine, J. Sakamoto, N. J. Dudney, Resolving the grain boundary and lattice impedance of hot-pressed $Li_7La_3Zr_2O_{12}$ garnet electrolytes. *ChemElectroChem* **1**, 375–378 (2014).
28. T. Lee, J. Qi, C. A. Gadre, H. Huyan, S.-T. Ko, Y. Zuo, C. Du, J. Li, T. Aoki, R. Wu, J. Luo, S. P. Ong, X. Pan, Atomic-scale origin of the low grain-boundary resistance in perovskite solid electrolyte $Li_{0.375}Sr_{0.4375}Ta_{0.75}Zr_{0.25}O_3$. *Nat. Commun.* **14**, 1940 (2023).
29. Y. Chen, Z. Lun, X. Zhao, K. P. Koirala, L. Li, Y. Sun, C. A. O'Keefe, X. Yang, Z. Cai, C. Wang, H. Ji, C. P. Grey, B. Ouyang, G. Ceder, Unlocking Li superionic conductivity in face-centred cubic oxides via face-sharing configurations. *Nat. Mater.* **23**, 535–542 (2024).
30. J. T. S. Irvine, D. C. Sinclair, A. R. West, Electroceramics: Characterization by impedance spectroscopy. *Adv. Mater.* **2**, 132–138 (1990).
31. Q. Zhou, B. Xu, P.-H. Chien, Y. Li, B. Huang, N. Wu, H. Xu, N. S. Grundish, Y.-Y. Hu, J. B. Goodenough, NASICON $Li_{1.2}Mg_{0.1}Zr_{1.9}(PO_4)_3$ solid electrolyte for an all-solid-state li-metal battery. *Small Methods* **4**, 2000764 (2020).
32. S. V. Patel, E. Truong, H. Liu, Y. Jin, B. L. Chen, Y. Wang, L. Miara, R. Kim, Y.-Y. Hu, Interrupted anion-network enhanced Li^+-ion conduction in $Li_{3+y}PO_4I_y$. *Energy Storage Mater.* **51**, 88–96 (2022).
33. A. Y. Toukmaji, J. A. Board, Ewald summation techniques in perspective: A survey. *Comput. Phys. Commun.* **95**, 73–92 (1996).
34. S. P. Ong, W. D. Richards, A. Jain, G. Hautier, M. Kocher, S. Cholia, D. Gunter, V. L. Chevrier, K. A. Persson, G. Ceder, Python materials genomics (pymatgen): A robust, open-source python library for materials analysis. *Comput. Mater. Sci.* **68**, 314–319 (2013).
35. Materials Project, https://next-gen.materialsproject.org/.
36. C. J. Pickard, F. Mauri, All-electron magnetic response with pseudopotentials: NMR chemical shifts. *Phys. Rev. B* **63**, 245101 (2001).
37. J. R. Yates, C. J. Pickard, F. Mauri, Calculation of NMR chemical shifts for extended systems using ultrasoft pseudopotentials. *Phys. Rev. B* **76**, 024401 (2007).
38. S. Yang, G. Li, L. You, J. Tao, C.-K. Loong, S. Tian, F. Liao, J. Lin, $Na_3[Ti_2P_2O_{10}F]$: A new oxyfluorinated titanium phosphate with an ionic conductive property. *Chem. Mater.* **19**, 942–947 (2007).
39. J. Hou, M. Hadouchi, L. Sui, J. Liu, M. Tang, W. H. Kan, M. Avdeev, G. Zhong, Y.-K. Liao, Y.-H. Lai, Y.-H. Chu, H.-J. Lin, C.-T. Chen, Z. Hu, Y. Huang, J. Ma, Unlocking fast and reversible sodium intercalation in NASICON $Na_4MnV(PO_4)_3$ by fluorine substitution. *Energy Storage Mater.* **42**, 307–316 (2021).
40. H. Bradtmüller, L. Zhang, C. C. de Araujo, H. Eckert, D. Moncke, D. Ehrt, Structural studies of $NaPO_3$–AlF_3 glasses by high-resolution double-resonance nuclear magnetic resonance spectroscopy. *J. Phys. Chem. C* **122**, 21579–21588 (2018).

Acknowledgments: We would like to thank X. Lin of MASSLab & X-Ray Crystallography Facility at Florida State University for assisting with the acquisition of the powder x-ray diffraction results. **Funding:** Y.-Y.H. received funding from the National Science Foundation grant DMR-1847038. Y.-Y.H. and Y.W. acknowledge funding from Samsung Advanced Institute of Technology. Y.-Y.H. also acknowledges that a portion of this work was performed at the National High Magnetic Field Laboratory, which is supported by National Science Foundation Cooperative Agreement nos. DMR-1644779 and DMR-2128556 and the state of Florida.
Author contributions: Conceptualization: Y.-Y.H. Methodology: Y.-Y.H. and R.K. Investigation: E.T., S.V.P., H.L., Y.C., V.L., C.Z., I.O., I.P.O., Y.J., B.T.J., L.J.M., V.P.D., H.G., R.K., Y.W., and Y.-Y.H. Supervision: Y.-Y.H. Writing—original draft: all authors. Writing—review and editing: all authors. **Competing interests:** The authors declare that they have no competing interests. **Data and materials availability:** All data needed to evaluate the conclusions in the paper are present in the paper and/or the Supplementary Materials.

Submitted 14 October 2024
Accepted 28 March 2025
Published 14 May 2025
10.1126/sciadv.adt7795